ADVANCED MATERIALS
www.advmat.de

Protonation Stimulates the Layered to Rock Salt Phase Transition of Ni-Rich Sodium Cathodes

Biwei Xiao, Yu Zheng, Miao Song, Xiang Liu, Gi-Hyeok Lee, Fred Omenya, Xin Yang, Mark H. Engelhard, David Reed, Wanli Yang, Khalil Amine, Gui-Liang Xu, Perla B. Balbuena,* and Xiaolin Li**

Protonation of oxide cathodes triggers surface transition metal dissolution and accelerates the performance degradation of Li-ion batteries. While strategies are developed to improve cathode material surface stability, little is known about the effects of protonation on bulk phase transitions in these cathode materials or their sodium-ion battery counterparts. Here, using $NaNiO_2$ in electrolytes with different proton-generating levels as model systems, a holistic picture of the effect of incorporated protons is presented. Protonation of lattice oxygens stimulate transition metal migration to the alkaline layer and accelerates layered-rock-salt phase transition, which leads to bulk structure disintegration and anisotropic surface reconstruction layers formation. A cathode that undergoes severe protonation reactions attains a porous architecture corresponding to its multifold performance fade. This work reveals that interactions between electrolyte and cathode that result in protonation can dominate the structural reversibility/stability of bulk cathodes, and the insight sheds light for the development of future batteries.

1. Introduction

Rechargeable intercalation batteries that convert between chemical and electrical energy through redox reactions almost certainly experience bulk structure and/or interface changes associated with the ion/electron transfer. The reversibility of the ion/electron transfer process and the material structure evolution hence dictate the rechargeability or cycle life of these batteries. Because the ion/electron diffusion and structure evolution are governed mainly by electrode materials' intrinsic properties and by dynamic interfacial reactions between electrolyte and electrode materials, maintaining the structural integrity and interfacial stability is essential to enable a high-performance battery.

Various types of surface coatings, material structure designs, and new electrolyte recipes and/or additives have been developed to control the electrode-electrolyte interaction.[1,2] Fundamental processes of the underlying mechanisms also have been investigated extensively.[3–7] However, research mainly has been focused on surface phenomena, including the compositions of the anode "solid-electrolyte interphase," "cathode electrolyte interphase," surface transition metal dissolution, and surface

B. Xiao, F. Omenya, X. Yang, D. Reed, X. Li
Energy & Environment Directorate
Pacific Northwest National Laboratory
Richland, WA 99352, USA
E-mail: xiaobiwei@grinm.com; xiaolin.li@pnnl.gov

Y. Zheng, P. B. Balbuena
Department of Chemical Engineering
Texas A&M University
College Station, TX 77843-3122, USA
E-mail: balbuena@mail.che.tamu.edu

Y. Zheng, P. B. Balbuena
Department of Chemistry
Texas A&M University
College Station, TX 77843-3122, USA

The ORCID identification number(s) for the author(s) of this article can be found under https://doi.org/10.1002/adma.202308380

DOI: 10.1002/adma.202308380

M. Song
Physical and Computational Sciences Directorate
Pacific Northwest National Laboratory
Richland, WA 99352, USA

X. Liu, K. Amine, G.-L. Xu
Chemical Sciences and Engineering Division
Argonne National Laboratory
9700 South Cass Avenue, Lemont, IL 60439, USA

G.-H. Lee, W. Yang
Advanced Light Source
Lawrence Berkeley National Laboratory
Berkeley, CA 94720, USA

G.-H. Lee
Department of Materials Science and Engineering
Dongguk University
Seoul 04620, Republic of Korea

M. H. Engelhard
Environmental Molecular Sciences Laboratory
Pacific Northwest National Laboratory
Richland, WA 99352, USA

P. B. Balbuena
Department of Materials Science and Engineering
Texas A&M University
College Station, TX 77843-3122, USA

reconstruction layer (SRL) of layered transition metal oxides.[1,8–12] The effect of electrolyte-electrode interaction on cathode bulk structure breakdown is largely overlooked, not to mention study of the underlying molecular processes.

Early studies on proton/lithium-ion exchange have indicated that protons from electrolyte can incorporate into the bulk of the layered lithium materials at charged states,[5–7] yet little has been elucidated about how the cathode bulk structure will evolve in successive cycles. Layered metal oxide cathodes, particularly Ni-rich materials have become promising candidates for increasing the energy density of rechargeable alkaline-ion batteries; hence, for performance improvement, there is urgent need to decipher why the interface is highly unstable with the electrolyte. Recently, the interaction of a Ni-rich cathode with an electrolyte at its grain boundaries has been linked to interparticle cracking in bulk spheres.[13] It also has been revealed that Ni-rich cathodes exhibit significantly different surface degradation rates in high concentration electrolyte, localized high concentration electrolyte (LHCE), and conventional carbonate electrolyte.[14–16] In this work, we reveal the molecular process governing Ni-rich sodium cathode/electrolyte interaction, including the protonation effect on the irreversible layered-rock-salt phase transition. We used $NaNiO_2$ as the representative cathode and conventional carbonate-based electrolyte and LHCE as model electrolyte systems. $NaNiO_2$ has the highest Ni amount, wide interlayer spacing after desodiation, and similar Na and proton occupation preferences on the trigonal prismatic sites, thus allowing for facile proton incorporation. It is therefore expected that $NaNiO_2$ should be able to present the most distinct effect. Conventional carbonate-based electrolyte and LHCE have dramatically different decomposition mechanisms and proton generation levels. Ab initio molecular dynamics simulation (AIMD) and systematic synchrotron X-ray and transmission electron microscopy (TEM) characterizations were integrated to elucidate the cathode structure degradation associated with bulk electrolyte decomposition as well as at the interfaces of pristine and charged cathodes. Carbonate electrolyte was found to involve more dehydrogenation reactions, and thus higher protonation of $NaNiO_2$ than LHCE, resulting in distinct oxygen loss and Ni migration. Consequently, carbonate electrolyte leads to more surface Ni reduction with thicker anisotropic SRLs than does LHCE, as well as the formation of a porous bulk architecture with more rock-salt NiO through spinel-like NiO_2 intermediate phases. The results provide new insight into the correlation of cathode fading and electrolyte-electrode interaction: electrolyte not only can affect the surface reconstruction and transition metal dissolution of cathode materials, but also accelerates the layered-rock-salt phase transition of the bulk cathode structure through mechanisms like generation and incorporation of protons. It opens new dimensions in engineering the cathode and electrolyte for future battery improvement.

2. Results and Discussion

2.1. Electrochemical Testing and Cathode Surface Characterization

The $NaNiO_2$ used in this work was synthesized through a common solid-state reaction.[17] The powder X-ray diffraction (XRD) pattern and Rietveld refinement in Figure S1a (Supporting Information) shows it is pure phase layered material with C2/m symmetry and an interlayer spacing of 5.32 Å. Scanning electron microscopy and high-angle annular dark-field scanning transmission electron microscopy (HAADF-STEM) results show that the particles in agglomerations have sizes of ≈2 µm and interlayer spacings of ≈5.3 Å (Figure S1b,c, Supporting Information).

The electrochemical performance of $NaNiO_2$ was tested between 2 and 4.2 V (vs Na/Na^+) in LHCE [5.1 M sodium bis(fluorosulfonyl)imide dissolved in dimethoxyethane (DME), diluted with bis(2,2,2-trifluoroethyl) ether (BTFE)] and carbonate-based electrolytes [1 M $NaPF_6$ dissolved in ethylene carbonate/propylene carbonate (EC/PC) at 1:1 vol%] (denoted EC/PC) under similar conditions (see details in Supporting Information). $NaNiO_2$ shows superior performance in LHCE to that in EC/PC from almost every aspect of electrochemical testing, including specific capacity, cycling stability, and rate performance (**Figures 1** and S2, Supporting Information). $NaNiO_2$ exhibits much higher initial charge and discharge capacities (183.1 and 136.9 mAh g^{-1}, respectively) in LHCE at 0.1C (1C = 120 mA g^{-1}) than those (152.8 and 108.9 mAh g^{-1}) in EC/PC electrolyte. The specific discharge capacity in LHCE after 100 cycles at 0.3C is ≈113 mAh g^{-1} (≈91.3% capacity retention from the fourth cycle), almost 2.5 times the value in EC/PC (≈45 mAh g^{-1}, 49% retention from the fourth cycle) (Figure 1a).

A close comparison of the charge/discharge curves (Figure 1b,c) shows that $NaNiO_2$ in LHCE exhibits a pair of plateaus >4.0 V during charging and ≈3.8 V during discharging (Figure 1b), which are absent in the charge/discharge curves obtained in EC/PC (Figure 1c). These plateaus, assigned to the distortion of O″3 to an O‴3 phase,[18,19] are highly reversible in LHCE even after 100 cycles. Because similar pattern of electrochemical performance difference also has been observed in the $NaNiO_2$||hard carbon full cells (Figure S3, Supporting Information), it reasonably infers that the performance difference in these electrolytes is from the distinct interaction of the electrolytes with the $NaNiO_2$ cathode rather than the Na metal.

Systematic soft X-ray absorption spectroscopy (sXAS) and TEM characterization were carried out to study the cathode surface structure evolution in different electrolytes. Ex situ Ni L_3-edge sXAS collected in total electron yield (TEY) mode yielded signal predominantly from the surface at several nanometers probing depth in this energy range; hence, this method is helpful to study the Ni redox behavior at the surface of $NaNiO_2$. Figure 1d,e presents the spectra obtained in various states of charge/discharge during the first cycle. In both electrolytes, $NaNiO_2$ shows a strong Peak I (Ni^{2+}) at OCV and a broad Peak II ($Ni^{3+/4+}$) that generally increase during charge and decrease during discharge. Peak II increased all the way to 4.2 V when the cathode was charged in LHCE, reflecting the continuous oxidization of surface Ni to $Ni^{3+/4+}$. The oxidation trend in EC/PC lasted only until the cathode was charged to 3.6 V, after which little Peak II change was observed. The result indicates that the surface reactivity/redox reversibility of $NaNiO_2$ is highly dependent on the electrolyte.

The difference in the surface redox reversibility in these electrolytes becomes even more striking after 10 cycles. The Ni L_3-edge sXAS spectra in Figure 1f,g shows repeated oscillation of the Peak II signal during charging and discharging of the electrode in LHCE but very small change in EC/PC. The distinct Ni reactivity

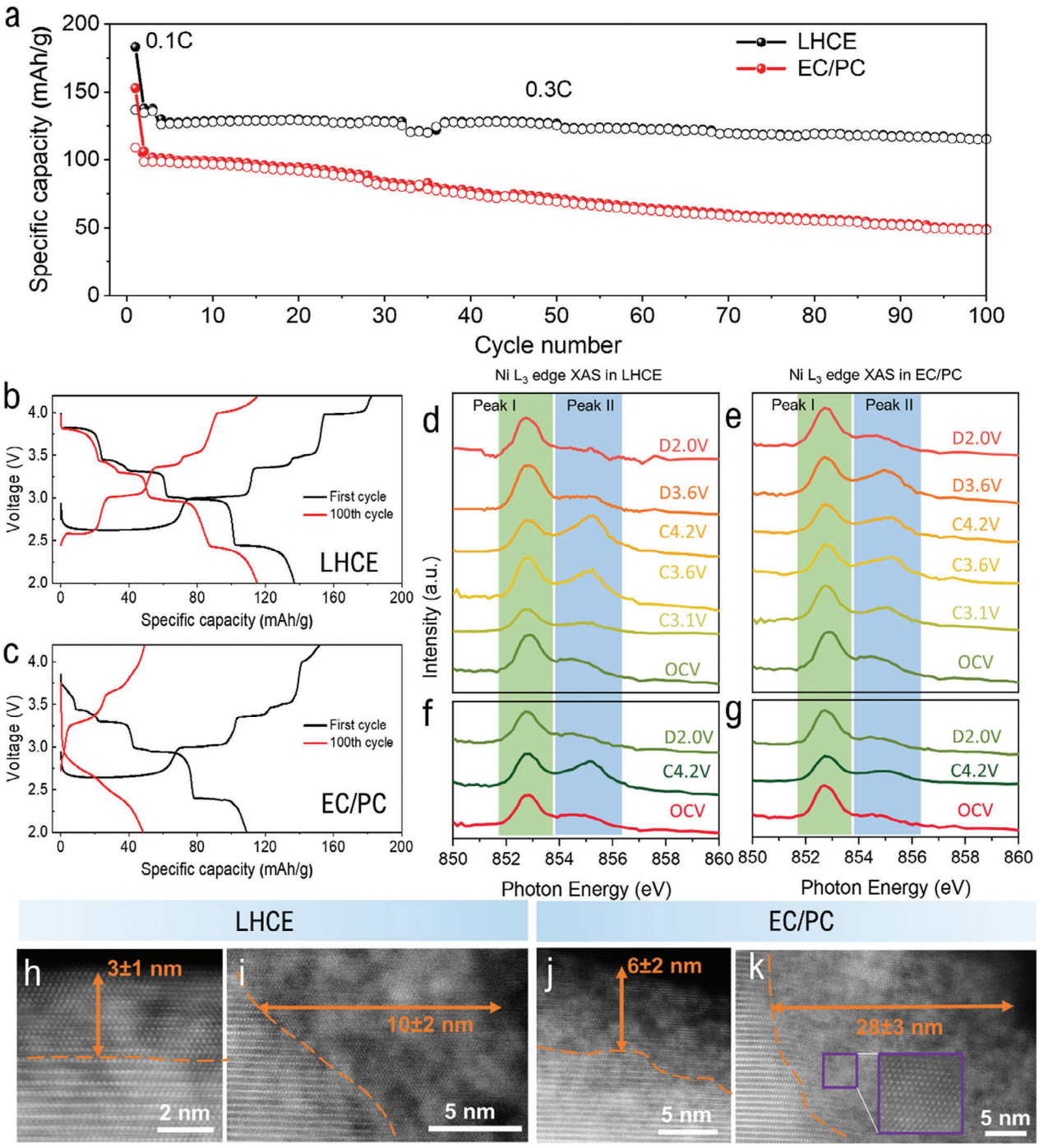

Figure 1. $NaNiO_2$ electrochemical performance and surface characterization. a) Half-cell cycling performances in LHCE and EC/PC (first cycle at C/10, subsequent cycles at C/3, 1C = 120 mA g^{-1}). b,c) Charge/discharge curves after the first and the 100th cycles in LHCE and EC/PC. d,e) Ex situ Ni L_3-edge XAS of $NaNiO_2$ cathodes in various charge/discharge states during the first cycle. f,g) Ex situ Ni L_3-edge XAS of $NaNiO_2$ cathodes at the open-circuit voltage (OCV), fully charged, and fully discharged states of the 10th cycle. h,i) HAADF-STEM images of the SRLs on $NaNiO_2$ after 10 cycles in LHCE. j,k) HAADF-STEM images of the SRLs on $NaNiO_2$ after 10 cycles in EC/PC.

indicates that the surface Ni in the sample cycled in EC/PC has almost become inactive after 10 cycles. HAADF-STEM images in Figure 1h–k and Figure S4 (Supporting Information) show the surface structures of the cathodes after being cycled 10 times in LHCE and in EC/PC. The particles display anisotropic formation of NiO-like rock salt SRL in both electrolytes. The SRLs formed in LHCE and in EC/PC, despite having different thicknesses, is thinner and denser on the facets parallel to the layers than on other facets. In LHCE, the SRL thickness is ≈3 nm along the layers and ≈10 nm across the layers. In EC/PC, the

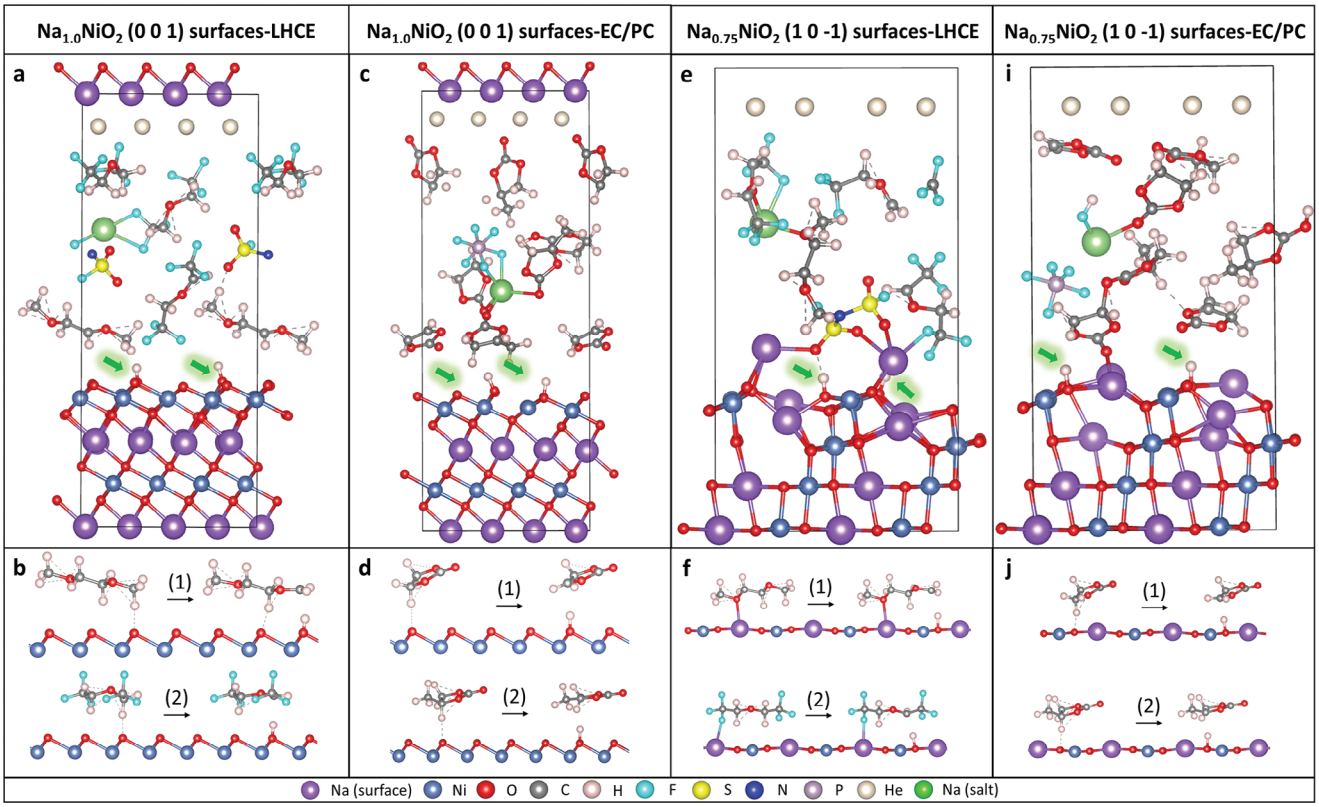

Figure 2. End configurations (top) and interfacial reactions (bottom) of electrolytes' (LHCE and EC/PC) decomposition on $NaNiO_2$ and $Na_{0.75}NiO_2$ surfaces. a–d) $Na_{1.0}NiO_2$ (0 0 1); e–j) $Na_{0.75}NiO_2$ (1 0 −1) surfaces after 10 ps AIMD simulations in electron-deficient environments. Color code: sodium (on surfaces), purple; nickel, dark blue; carbon, gray; oxygen, red; hydrogen, light pink; fluorine, light blue; sodium (from salt), green; sulfur, yellow; nitrogen, blue; phosphorus, light purple; helium, white. Green arrows in each simulation cell highlight the locations of surface protonation.

SRL thickness has increased to ≈8 nm perpendicular to the layers and ≈28 nm along the layers; this has essentially exceeded the probing depth of sXAS in TEY mode, and thus is consistent with the subtle Peak II signal change upon charging and discharging. Such anisotropic SRLs formation also infers that morphology control of the primary particles to rod-like structure with higher (003) plane benefits the cycling stability.

2.2. Understanding Electrolyte Decomposition and Surface Protonation

To investigate how electrolytes' reactivities lead to SRL formation, we carried out computational studies on bulk LHCE and EC/PC decomposition and electrolyte interfacial reactions on $NaNiO_2$ surfaces. To model the effect of an electrified cathode interface, a number of electrons were removed from the simulation cell to mimic the electron-deficient environment in the bulk and near the cathode surface.[20] The simulation scheme is shown in Figure S5 (Supporting Information), and the computation details are in the Supporting Information. Figure S6 (Supporting Information) summarizes the reaction mechanisms and charge evolution of bulk electrolyte oxidative decomposition. Figures S7 and S8 (Supporting Information) show the instantaneous charge analysis and energetics values are listed in Table S1 (Supporting Information). In general, the dissociation of DME and BTFE is the primary decomposition path of LHCE, whereas EC/PC prefers to undergo proton-transfer reactions.

We incorporated $NaNiO_2$ cathode surfaces into our model to investigate the molecular processes of cathode-electrolyte interfacial reactions. Two facets, (0 0 1) and (1 0 −1), were selected to represent possible orientations of Na^+ migration on a $NaNiO_2$ cathode. As seen in Figure S5c,d (Supporting Information), (1 0 −1) surfaces cross the sloped Na^+-moving channel, whereas (0 0 1) surfaces are parallel to the Na layer with NiO_2 (O—Ni—O) units exposed on the top, which impedes Na^+ migration. **Figure 2** and Figures S9 and S10 (Supporting Information) demonstrate the initial and final configurations and reaction mechanisms of LHCE and EC/PC decomposition on pristine and charged $NaNiO_2$ surfaces. Our interfacial simulations of fully discharged or primitive $Na_{1.0}NiO_2$ surfaces revealed that both LHCE and EC/PC are still more reactive on (0 0 1) surfaces (Figure 2a–c) than on (1 0 −1) surfaces (Figures S9b and S10b, Supporting Information): no interfacial reactions was detected on (1 0 −1) surfaces (Figures S9c and S10c, Supporting Information), while surface protonation was detected on (0 0 1) surfaces (Figure S11, Supporting Information). The deprotonation of DME is shown with the loss of the terminal hydrogen atom to a surface O (O_s) atom, which leads to the formation of a hydroxyl (—OH) group on (0 0 1) surfaces, as seen in Figure 2b. And BTFE undergoes either deprotonation when it is initially near the surface, or dissociation when it is in the middle of the simulation cell. EC and PC follow

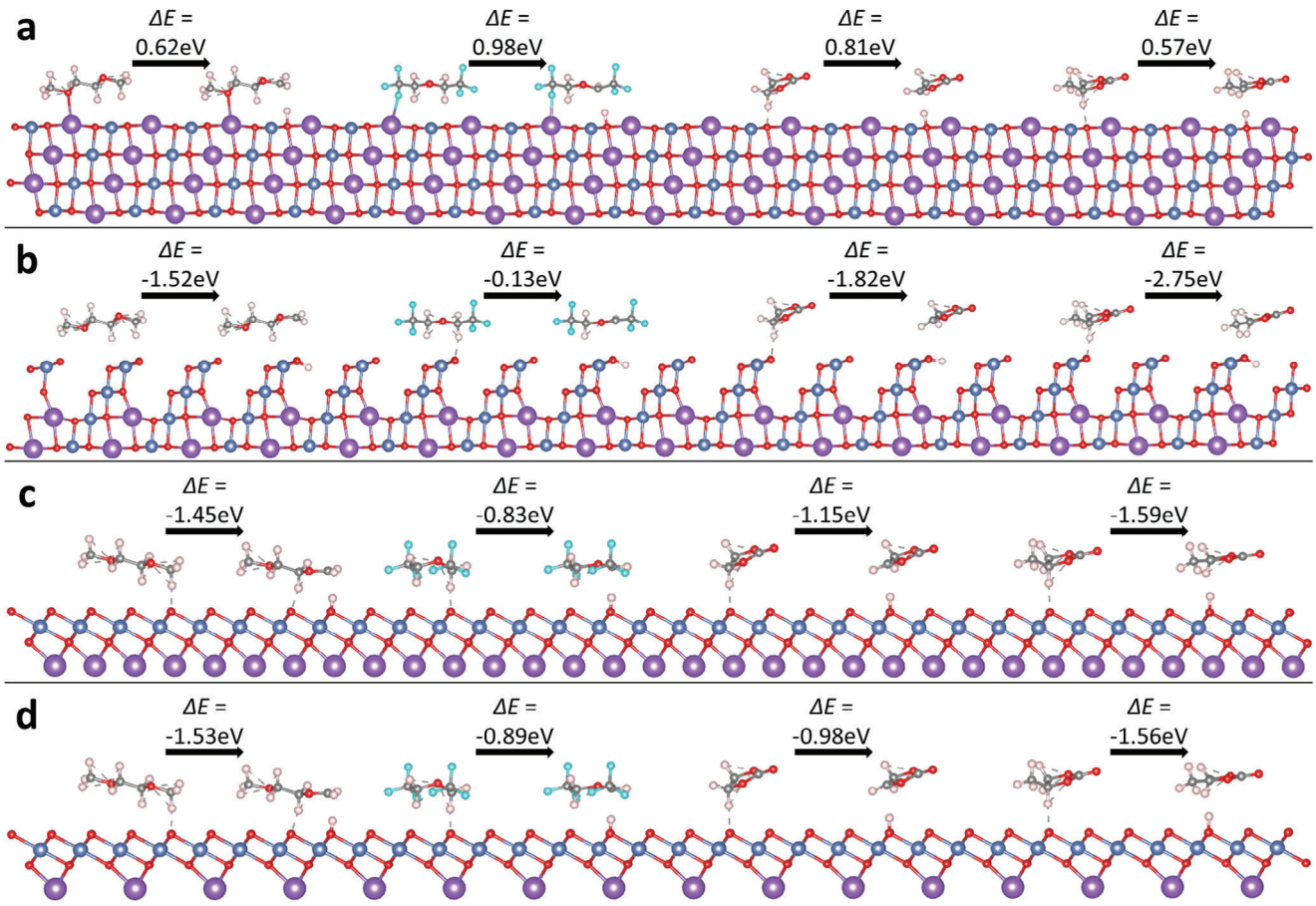

Figure 3. Reaction energies (in eV) of deprotonation of single electrolyte molecules (left to right: DME, BTFE, EC, PC) on a) $NaNiO_2$ (1 0 −1); b) $Na_{0.5}NiO_2$ (1 0 −1); c) $NaNiO_2$ (0 0 1); d) $Na_{0.5}NiO_2$ (0 0 1) surfaces. The color code is the same as in Figure 2.

a similar mechanism by transferring the ethylene protons to the surfaces, as shown in Figure 2d. Compared to the proton-transfer reactions (ethylene proton to carbonyl oxygen (O_c) or fluorine anion) within bulk EC/PC electrolytes (Figure S6e, Supporting Information), the formation of surface protonation indicates that O_s atoms are stronger oxidizing agents than O_c atoms of carbonate; thus, protons are more likely abstracted by oxide surfaces.[21]

Considering the effect of cathode desodiation during the charging process, electrolyte decompositions on partially-desodiated $Na_{0.75}NiO_2$ (001) (Figure 2e–i), $Na_{0.75}NiO_2$ (1 0 −1) (Figures S9e and S10e, Supporting Information) and $Na_{0.5}NiO_2$ (1 0 −1) (Figures S9h and S10h, Supporting Information) surfaces were also investigated. LHCE and EC/PC were obviously more reactive when surfaces were partially charged, as evidenced by the identification of both electrolytes' deprotonation shown in Figure 2 and Figures S9 and S10 (Supporting Information). Since electrolyte deprotonation is facilitated by Na^+ dissolution (different sodiation states), it is worthwhile to compare the reaction energies of electrolyte deprotonation on $Na_{1.0}NiO_2$ and $Na_{0.5}NiO_2$ (1 0 −1) surfaces. Unlike in AIMD, accurate energetics calculations were performed in electron-neutral environments (no electron removal from the simulation cell).[22] **Figure 3** shows the schematics and Table S2 (Supporting Information) shows the detailed charge analysis details. As shown in Figure 3a, all proton-transfer reactions on $Na_{1.0}NiO_2$ (1 0 −1) surfaces were thermodynamically unfavorable, which explains why no deprotonation reactions are detected in the AIMD simulations on $Na_{1.0}NiO_2$ (1 0 −1) surfaces. However, when the surfaces were partially charged, the reactivities of electrolyte deprotonation were clearly increased, which agrees with results of our AIMD simulations that electrolytes are more reactive on the desodiated/charged surfaces. The reaction energies were calculated to be negative on $Na_{0.5}NiO_2$ (1 0 −1) surfaces (shown in Figure 3b), with PC > EC > DME > BTFE. As EC/PC was more reactive than LHCE and considering the results in Figure 1, it is also reasonable to believe that the lower reactivity of deprotonation behavior in LHCE is the reason that SRL formation has been largely suppressed, resulting in more stable cycling. Therefore, minimizing electrolyte deprotonation by using less reactive LHCE is an efficient strategy for achieving better capacity retention of Ni-rich cathodes.

In comparison, the electrolyte deprotonation on $NaNiO_2$ (0 0 1) surfaces was calculated to be thermodynamically favorable, however, there was almost no difference in energy values for the process of charging (desodiation), as seen in Figure 3c,d. This can be explained by the changes of the exposed layers (where the proton-transfer reactions happen) of the $NaNiO_2$ (1 0 −1) and (0 0 1) surfaces upon charging. The O atoms were the only exposed layer

of (0 0 1) surfaces and desodiation could barely change the structural composition of the exposed layers. In contrast, the exposed layer of the $NaNiO_2$ (1 0 −1) surface consists of Na, O, and Ni atoms, and when it was charged, Na atoms were removed from the exposed layer, thus leaving more exposed O atoms on the surfaces as protonation sites. This is in good agreement with the HAADF-STEM results in Figure 1, which indicate thinner SRLs form at facets parallel to the layers, where the surface reactivity won't be increased during the charging process.

Finally, we calculated the reaction barriers of electrolyte deprotonation on $Na_{0.5}NiO_2$ (1 0 −1) surfaces to determine the kinetic favorability of the reactions. As seen in Figure S12 (Supporting Information), the deprotonation of DME is spontaneous, as indicated by the negative energy value at state 1. BTFE deprotonation has the highest kinetic barriers of 2.58 eV, which indicates that BTFE deprotonation is kinetically unfavorable. As BTFE contributes to the major component of LHCE solutions (due to large ratio of diluents), the stability of LHCE is increased, which corroborates our observation of thinner SRLs formed in LHCE, as shown in Figure 1. The kinetic barrier of EC deprotonation is 0.82 eV and PC deprotonation is spontaneous (negative energy value at every transition state), which means PC is more reactive than EC.

2.3. Proton-Induced Ni Reduction and Migration

The above results for LHCE and EC/PC decomposition suggest that an electrolyte more stable against deprotonation was less reactive on $NaNiO_2$ surfaces. However, the underlying mechanisms of the way protonation induces surface and bulk structure degradation are still poorly understood. To elucidate them, we first examined the oxidation states of Ni atoms upon proton transfer by using DME deprotonation on $NaNiO_2$ (1 0 −1) surfaces as an example. The oxidation states were analyzed by the change of local magnetic moments (Table S2, Supporting Information), and it was revealed that a Ni atom (highlighted in yellow in Figure S13a, Supporting Information) was reduced from the oxidation state from +3 to +2 when a proton was transferred to its neighboring O atom, forming the —OH group on the surface. As protonation continues during the cathode desodiation, the reduction of Ni atoms also remains while some of the Ni-ions increase to high oxidation states, from Ni^{3+} to Ni^{4+}, as shown in Figure S13b (Supporting Information). Meanwhile, the Ni—O bond length increased from 1.914 to 2.161 Å (1.862–1.969 Å) when protons were attached to O_s atoms on $Na_{1.0}NiO_2$ ($Na_{0.5}NiO_2$) (1 0 −1) surfaces, which weakened the Ni—O bonding.

Because the spontaneous reduction of Ni^{3+} to Ni^{2+} has been acknowledged as a source of phase transition of $LiNiO_2$,[23,24] it is reasonable to hypothesize that the identified Ni reduction and weakening of the Ni—O bond might also cause the instability of $NaNiO_2$. To validate this, we built a model using partially desodiated $Na_{0.25}NiO_2$ (1 0 −1) surfaces with some extent of surface protonation (H content = 0.25), as shown in **Figure** 4a–c. Because $NaNiO_2$ will undergo a broad phase transition from a monoclinic (in C2/m symmetry) to rhombohedral (in R-3m symmetry) structure at temperatures >243 °C during heating treatment,[25] the C/2m structure was used to investigate the structural transformation of $Na_{0.25}H_{0.25}NiO_2$ (1 0 −1) surfaces at low temperature. As shown in Figure 4a, protons hopping between O_s atoms (highlighted in green circles) were observed when protons were initially attached to O_s atoms on each side of NiO_2 units. After 1.7 ps of AIMD simulation at $T = 450$ K, some protons were transferred to O_s atoms of neighboring NiO_2 units and to O_s atoms on subsurface layers, which indicates the mobility of surface protons.

Meanwhile, Ni migration (highlighted in blue triangles) from its original position (transition metal layer) into a Na vacancy site (desodiation channel) was identified, as shown in Figure 4b. Similar Ni migration in $LiNiO_2$ was considered to provide nuclei for phase transitions of layered NiO_2 to spinel-like NiO_2, which destroys active Li sites and results in a gradual capacity decline with cycling.[24] Therefore, it is reasonable to believe that protons could also induce the similar phase transition of $NaNiO_2$, because there is no such phenomenon found in proton-free surfaces even at the high temperature of $T = 670$ K, as shown in Figure S14 (Supporting Information). And when Ni migrates, the Na^+-moving pathways are blocked; thus, the number of active Na^+ ions also decrease.

Considering that protons are mobile, we built another $Na_{0.25}H_{0.25}NiO_2$ (1 0 −1) surface model with protons attached to O_s atoms on neighboring NiO_2 units, as shown in Figure S15 (Supporting Information). The Ni migration was also observed after 1 ps of AIMD simulation at $T = 450$ K; meanwhile, hopping of protons to other O atoms was also seen, resulting in the formation of H—O—H bonds, with O bonding with a surface Ni atom. When the simulation temperature was elevated to $T = 600$ K (Figure 4c), H_2O was found to release from the surface by breaking the Ni—O bond, triggering the structural degradation of $NaNiO_2$. Since it was reported that at the high temperature of $T = 600$ K, bulk $NaNiO_2$ adopts an R-3m symmetry and oxygen gas evolves on R-3m $LiNiO_2$ (0 1 2) surfaces,[26] we also investigated the thermal stability of R-3m $Na_{0.25}NiO_2$ (0 1 2) surfaces. As shown in Figure 4d, the formation of O—O bonding and the release of O_2 were observed after only 0.5 ps of AIMD simulation at $T = 600$ K. This reveals that $NaNiO_2$ was unstable upon heating, and the structural degradation can be summarized by the following equation:

$$NiOOH \rightarrow NiO + O_2 + H_2O \quad (1)$$

Therefore, we believe that protonation induces quick degradation of the surfaces of $NaNiO_2$ cathode materials.

Because there are many other sources of proton generation than the vigorous decomposition of electrolyte solvent,[8] and it has been known that protonation can happen to layered metal oxides in the bulk,[7,27] we then examined the effect of protons on $NaNiO_2$ crystal structure. Figure 4e illustrates the bulk structure of $NaNiO_2$ upon desodiation and proton intercalation. Protons are bonded with O atoms and stay close to Na vacancy sites. The relationship between the H content and the c-axis lattice constant is shown in Figure 4f. It is clear that as increasing numbers of protons are aligned with the $NaNiO_2$ crystal, the c lattice parameter decreases. Along with the desodiation process, protonated $NaNiO_2$ is expected to undergo a lattice shrinkage. Once the lattice shrinks, the ion transfer capability will deteriorate further,[7,28] which explains the more severe capacity loss in EC/PC solutions, as shown in Figure 1a, as EC/PC involves more proton generation.

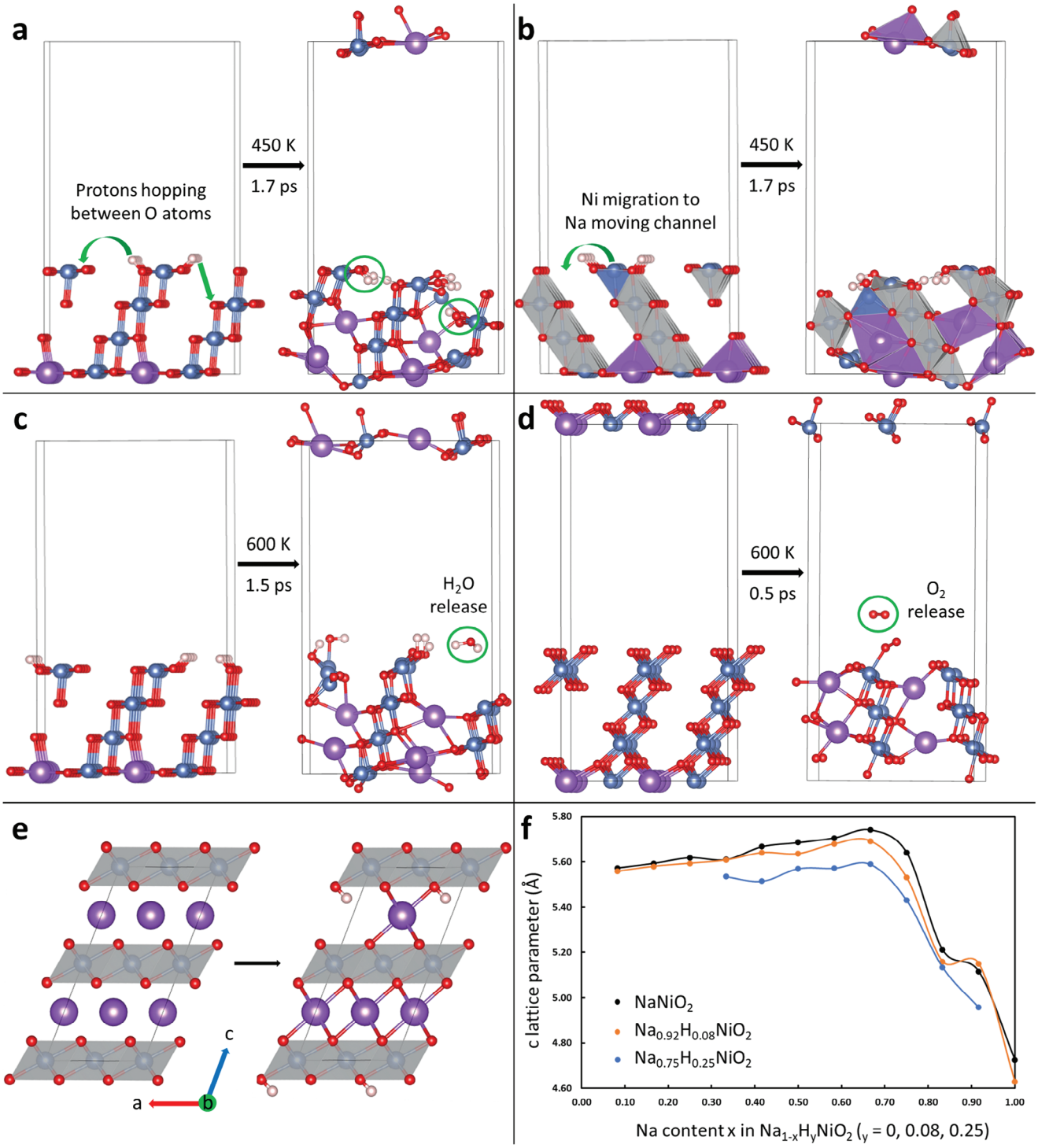

Figure 4. Effect of protonation on $NaNiO_2$ structure degradation. a) Surface protons hopping between O atoms at C2/m $Na_{0.25}H_{0.25}NiO_2$ (1 0 −1) surfaces after 1.7 ps of AIMD simulation at $T = 450$ K. b) a Ni atom at C2/m $Na_{0.25}H_{0.25}NiO_2$ (1 0 −1) surfaces migrating to desodiation channel after 1.7 ps of AIMD simulation at $T = 450$ K. c) H_2O release from C2/m $Na_{0.25}H_{0.25}NiO_2$ (1 0 −1) surfaces after 1.5 ps of AIMD simulation at $T = 600$ K. d) O_2 release from R-3m $Na_{0.25}NiO_2$ (0 1 2) surfaces after 0.5 ps of AIMD simulation at $T = 600$ K. e) Illustration of proton intercalation in partially desodiated $NaNiO_2$ crystal structure (in C2/m symmetry). f) Relationship between Na content (x) and c lattice parameter in desodiated $Na_{1-x}NiO_2$ and protonated $Na_{1-x}H_yNiO_2$ (y: H content) crystal. Color code is the same as in Figure 2.

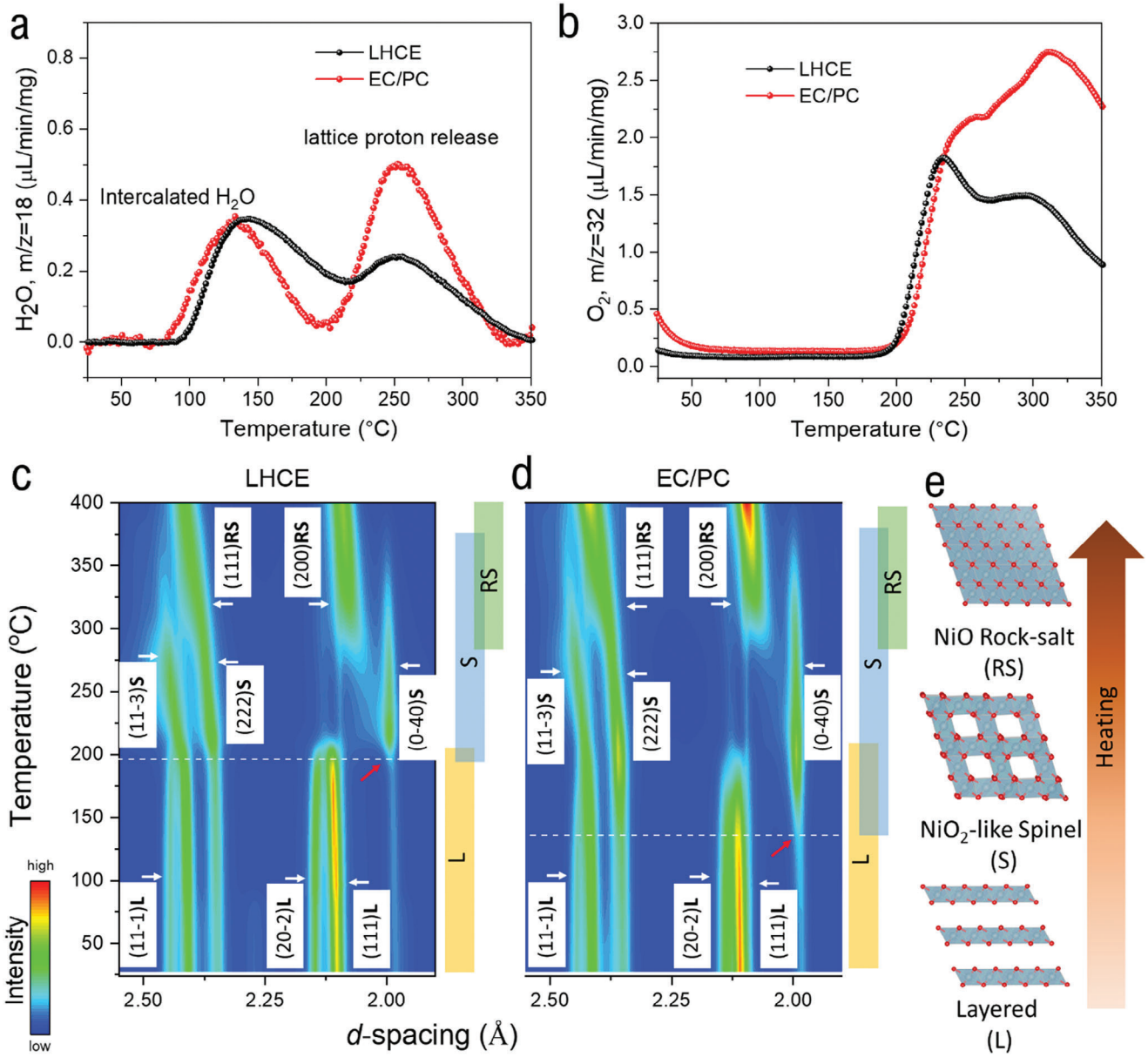

Figure 5. a) Mass spectrometry of H_2O release (mass-to-charge ratio m/z = 18) of $Na_{1-x}NiO_2$ charged in LHCE and in EC/PC upon heating. b) Mass spectrometry of O_2 release (m/z = 32) of $Na_{1-x}NiO_2$ charged in LHCE and in EC/PC upon heating. c) In situ heated high-energy XRD of $Na_{1-x}NiO_2$ charged in LHCE. d) In situ heated high-energy XRD of $Na_{1-x}NiO_2$ charged in EC/PC. e) Schematic illustration showing the phase transition of charged $Na_{1-x}NiO_2$ upon heating.

2.4. Protonation and Bulk Structure Transformation

Mass spectrometry coupled with in situ-heated high-energy XRD was performed on $Na_{1-x}NiO_2$ samples after the first charge to 4.2 V in the same two electrolytes to verify the presence of a lattice proton and its effect. **Figure** 5a shows two water-release peaks; the one positioned at 100–200 °C corresponds to intercalated water molecules, and the second peak, centered ≈250 °C, is well acknowledged as reflecting the removal of a lattice proton.[27,29] (See detailed discussion about the water peaks in Supporting Information.) Thermogravimetric analysis of layered $Ni(OH)_2$ and NiOOH also shows that the temperature is in the same range as where these materials lose their lattice protons in the form of water (Figure S16a–c, Supporting Information). The substantially stronger peak for the EC/PC sample than the LHCE sample also is consistent with our simulation results on electrolyte decomposition and $NaNiO_2$ protonation: EC/PC deprotonate to a greater degree both in bulk electrolyte and on the cathode surface (Figures 2 and 3; Figure S6, Supporting Information). The possible hydrolysis of $NaPF_6$ also generates more protons, leading to considerable protonation of $NaNiO_2$ cathodes. Because the lattice oxygen, once protonated, might also be destabilized, leading to potential oxygen gas loss behavior, oxygen gas release was investigated. Figure 5b shows the oxygen gas release upon heating

of the two samples. The onset oxygen gas release temperature is higher for the sample charged in EC/PC than that in LHCE (210 vs 200 °C), which is possibly because oxygen was mainly lost in the form of water in EC/PC at the beginning, thus postponing the O_2 gas release. The oxygen release peak ≈300 °C is related to a phase transition, which will be further addressed in later discussions on in situ heated XRD. We have also collected the CO_2 emission as shown in Figure S16d (Supporting Information), the LHCE sample still displays less CO_2 emission, indicating more stable structure compared with the EC/PC sample.

Figure S17 (Supporting Information) shows the d-spacing of the initial $Na_{1-x}NiO_2$ desodiated to 4.2 V in each electrolyte. The position of the (003) peak has a lower value in EC/PC than in LHCE, corroborating Figure 4f in that a larger number of protons in the structure leads to a smaller d-spacing along the c-axis. Figure 5c,d presents the contour plot of the in situ heated XRD, and the line plots are shown in Figure S18 (Supporting Information). While intercalated water was observed in the samples at room temperature, it was not from the electrolyte because the in situ XRD of the $NaNiO_2$ that has been previously cycled ex situ 50 times in LHCE (Figure S19, Supporting Information) does not show any expansion >7.0 Å. A trace amount of intercalated water was just unavoidable during preparation of the sample for heating. Karl Fischer titration showed that the water concentration in LHCE and EC/PC is 24.2 and 16.1 ppm, respectively, which are considered similar level of average water content for liquid electrolytes. The fact that similar $NaNiO_2$ electrodes showed different fading behavior in the electrolytes with similar water content supports that the protonation effect is mainly from electrolyte decomposition instead of the trace amount of H_2O in air, in electrode or in electrolyte. As shown in Figure 5c,d, the samples charged in LHCE and in EC/PC show similar layered structures before heating and rock salt structures after heating to >300 °C. The initial heating process also shows unchanged layered-phase diffractions in both cases. However, several distinct phase transition behaviors were observed, indicating that a different protonation degree affects the structural degradation behavior upon heating. First, the decrease of the (111) layered peak intensity and the commencement of the $(0\bar{4}0)$ peak of spinel-like NiO_2 ≈1.98 Å happen at a quite low temperature of 145 °C in the EC/PC sample but ≈200 °C in the LHCE sample (marked with red arrows in Figure 5c,d). Neither lattice-proton nor oxygen gas release was initiated at such a low temperature in the EC/PC sample (Figure 5a,b). Second, in the EC/PC sample, the layered and spinel phases coexist over a significant range until the temperature reaches 200 °C, where the (111) layered peak disappears. The LHCE sample shows a quick drop of the (111) layered peak intensity ≈200 °C, with the simultaneous emergence of spinel phase. Third, the transition from spinel to rock salt phase starting at ≈300 °C corresponds to the second oxygen release event tips in Figure 5b; its relative diffraction intensity is significantly stronger in EC/PC than that of LHCE.

Considering the correlation of the temperatures (145, 200, and 300 °C) of major phase transitions and the release of O_2 gas and lattice protons in water, it is reasonable to conclude that the layered-to-spinel and then rock salt phase transition in the LHCE sample is largely triggered solely by the loss of lattice oxygen following the process illustrated in Figure 5e.[30] For the EC/PC sample, however, the low-temperature layered-to-spinel phase transition without loss of lattice oxygen indicates that the lattice protons have destabilized the Ni and prompted its migration to the alkaline layer to form a spinel phase, consistent with the computational result in Figure 4. The oxygen loss from the EC/PC sample happens when most of the layered phase has become spinel at ≈210 °C.

The above results on different structural degradation behaviors upon heating and contrasting Ni migration energies also make it safe to infer that protonation may affect the energy required for bulk structure transition and the degradation pathways over long-term battery cycling. The $NaNiO_2$ cathodes, which show noticeably different capacity retention after 100 cycles in LHCE and in EC/PC electrolyte, were characterized. **Figure 6** shows dramatically different SRL evolution and bulk structure degradation for the two electrolytes. Figure 6a–d is STEM images and electron energy loss spectroscopy (EELS) maps taken on the surface of some $NaNiO_2$ particles cycled in LHCE and in EC/PC. The low magnification STEM images and representative EELS spectra were shown in Figure S20 (Supporting Information). The LHCE sample (Figure 6a) shows a much thinner SRL layer than the EC/PC sample (Figure 6c). The EELS maps in Figure 6b–d shows the Ni^{2+} layer is ≈20 nm thick on the surface of the LHCE sample but hundreds of nanometers deep in the EC/PC sample. The anisotropic SRL feature remains after long-term cycling in LHCE. Figure S21 (Supporting Information) shows a typical STEM image with a ≈2 nm SRL along the layers and a ≈20 nm SRL perpendicular to the layers. Comparing the results from a pristine electrode and an electrode after 10 cycles, the SRL thickness along the layers changed very little but it doubled in the direction perpendicular to the layers.

For the bulk structure evolution, the LHCE sample displays mainly the formation of cracks along the layer direction (Figure 6e). It is similar to many layered lithium and sodium materials and also can be ascribed to the gliding of layers upon ion deintercalation and reintercalation.[31–33] HAADF-STEM was used to examine the crystal structure of the particles. Three representative regions (marked with yellow, red, and purple boxes in Figure 6e) of a cracked particle were closely scrutinized using HAADF-STEM and selective area electron diffraction (SAED). Figure 6f–h shows rock salt crystallites at the particle surface, a rock-salt-layered junction at the surface of a crack interface and regular layered structure in the bulk. The crystal structures were indexed in the inset SAED patterns. The intraparticle cracking, which introduces fresh surfaces to further react with the electrolyte and has been considered as a major capacity fading mechanism to many layered oxide cathodes of Li-ion batteries,[1] induces a rock salt layer of only ≈2 nm to the $NaNiO_2$ cathode cycled in LHCE. It did not cause noticeable capacity fading considering the good capacity retention shown in Figure 1.

The EC/PC sample experiences severe bulk structure breakdown after 100 cycles. Figure S22 (Supporting Information) shows the formation of randomly oriented cracks and thick rock salt layers composed of discrete nanodomains. While some particles have parts with retained layered structures, many were collapsed and had rock salt phase throughout the bulk particle with simultaneous pore development. Figure 6i is a HAADF-STEM image of a typical region adopted from the bulk part of a particle. Discrete rock salt nanodomains with pores of several nanometers are present. 3D electron tomography is used to present a

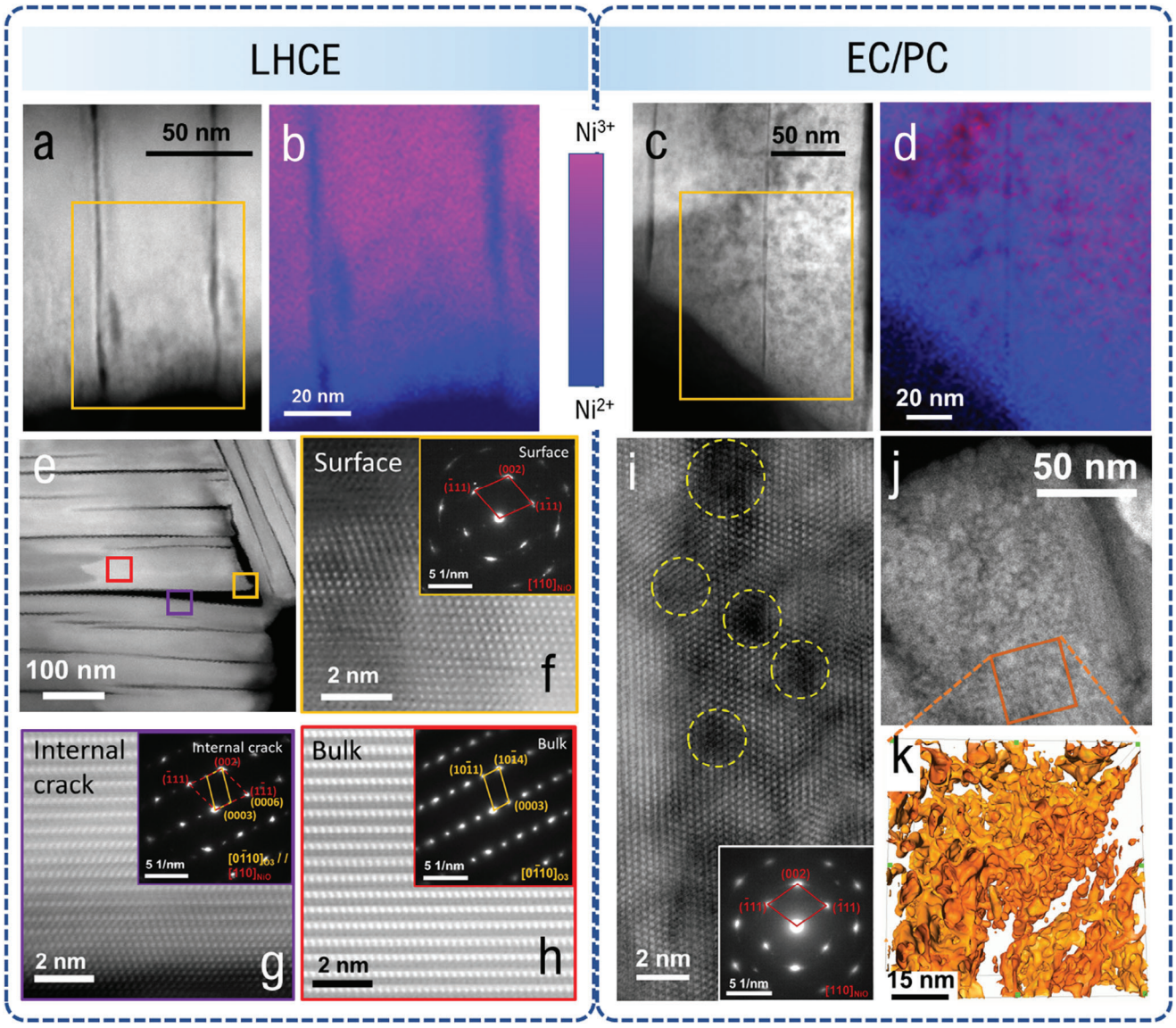

Figure 6. Structural characterization of long-term cycled $NaNiO_2$. a–d) HAADF-STEM image and corresponding EELS mapping of $NaNiO_2$ cycled in LHCE and in EC/PC for 100 cycles. e) STEM image of a particle with intragranular cracks at low magnification and three different regions examined with HAADF-STEM and SAED. f–h) HAADF-STEM images of the surface region (yellow) showing rock-salt structures, internal crack region (purple) showing mixed rock-salt/layered structures and bulk region (red) showing layered structures (insets: SAED patterns) i) HAADF-STEM image of a typical region of $NaNiO_2$ cycled in EC/PC 100 times showing discrete rock-salt nanodomains (some of the pores are marked with yellow dashed circles). j) Low magnification HAADF-STEM image showing the location of the 3D tomography reconstruction region in (k). k) Electron tomography 3D surface rendering of pores in the EC/PC sample.

straightforward view of these nanopores. Figure 6j shows the morphology of a particle after focused ion beam processing and Figure 6k is a typical 3D tomographic reconstruction image of a cuboid (70 nm × 70 nm × 35 nm) from the center of the particle (more figures showing the location of the region of interest and 3D electron tomography reconstruction are shown in Figure S23 and Videos S1 and S2, Supporting Information). As shown in these images, the nanodomains around the voids mostly are interconnected, though some are detached from the particle and appear to be isolated. A random crack, which was also employed as a contrast reference during reconstruction, is observed at the bottom right of Figure 6k. XRD patterns of $NaNiO_2$ cycled in both electrolytes for 100 times (Figure S24, Supporting Information) also show that the rock salt phase has developed largely in EC/PC sample. The layered structure, however, has been well preserved in LHCE. Although loss of oxygen from anionic redox activity and oxidation of tetravalent Ni to the lattice oxygen have been known to create pores,[34–36] it is not applicable to our case. We performed mapping of resonant inelastic X-ray scattering (mRIXS) of the O *K*-edge for electrodes charged in conventional and LHCE electrolytes (Figure S25, Supporting Information). It has been established that lattice oxidized oxygen displays

fingerprint features in O-*K* mRIXS, especially through a sharp feature at 531 eV (excitation energy) and 524 eV (emission energy),[37–39] while very weak or no signal was observed for electrodes cycled in LHCE and in EC/PC electrolytes. The $NaNiO_2$ demonstrates more tetravalent Ni in the sample charged in LHCE (Figure 1d–f). It is believed that the pores are related to proton-induced oxygen loss after long term cycling, which leads to Ni migration and rock-salt phase development. Moreover, water is generated during this process, which exacerbates the phase transition.

Extensive protonation of $NaNiO_2$ and subsequent layered structure breakdown and particle pulverization is the main reason for the low specific capacity and the poor cycling stability in EC/PC electrolyte. This is not a rare case; proton incorporation into the bulk structure of lithium transition metal oxides through proton-Li exchange has been known for years.[5,40–42] Yet, the bulk structural breakdown of layered lithium cathodes was not investigated/observed. From one aspect, that was not the focus of the previous research. On the other hand, $NaNiO_2$ has more phase transitions and larger interlayer spacing than lithium cathodes, which favors proton and Na exchange at trigonal prismatic sites.[42] For layered Li cathodes, forming the trigonal prismatic sites would require extra layer gliding, making it less likely to happen. Nonetheless, once incorporated, despite only possibly happening locally, these protons could still act as defective sites that may trigger local structural change.[43]

3. Conclusion

Fundamentals of the protonation of a Ni-rich sodium cathode and its effect on surface phase reconstruction and bulk structural breakdown have been elucidated using model systems of $NaNiO_2$ in carbonate-based electrolytes and in LHCE. While conventional studies have shown that protonation leads to transition metal dissolution and protons can exchange with Li ions in lithium cathodes, our study clearly reveals that its role has been considerably underrated, if not missed, for Ni-rich sodium cathodes. The different bulk electrolyte decomposition and reactions at different cathode surfaces result in distinct protonation degrees. While anisotropic SRL formation was observed in $NaNiO_2$ cycled in either electrolyte, the high protonation degree of the layered cathode in carbonate electrolyte resulted in a thicker SRL and more heavily reduced Ni^{2+} than that in LHCE. More importantly, the incorporated protons may destabilize the oxygen surrounding the Ni-ions, thus facilitating the transition metal migration to alkaline layers without necessary oxygen loss, leading to vigorous phase transition and the formation of porous rock-salt nanodomains in the bulk and disordered cracks irrelevant to regular layer gliding. This phenomenon has been previously overlooked when assigning the reasons for layered-spinel/rock-salt phase transition.[44] Such structural breakdown subsequently is responsible for the poorer electrochemical performance of $NaNiO_2$ cycled in EC/PC electrolyte compared with the LHCE electrolyte. The results provide new insight into the correlation of electrolyte and material surface-to-bulk structural degradation. Electrolyte not only can affect the surface reconstruction and metal dissolution of cathodes, but also dictates the structural reversibility/stability of the bulk cathode through mechanisms like generation and incorporation of protons. It also calls for more detailed studies on proton-related structural transitions in layered materials and engineering Ni-rich cathodes and electrolytes to attain better cycling performance.

Supporting Information

Supporting Information is available from the Wiley Online Library or from the author.

Acknowledgements

B.X. and X.L. would like to thank the U.S. Department of Energy (DOE) Office of Electricity (Contract No. 70247A) for their support. Pacific Northwest National Laboratory is a multiprogram laboratory operated by Battelle Memorial Institute for the DOE under Contract DE-AC05-76RL01830. Y.Z. and P.B.B. acknowledge financial support from the Department of Chemical Engineering at Texas A&M University through the Mike O'Connor Chair I, and computational resources from High-Performance Research Computing at Texas A&M University. Research at Argonne National Laboratory was funded by the DOE Vehicle Technologies Office (VTO). Support from T. Duong of the VTO was gratefully acknowledged. Use of the Advanced Photon Source, an Office of Science User Facility operated for the DOE Office of Science by Argonne National Laboratory, was supported by DOE under contract no. DE-AC02-06CH11357. Soft X-ray experiments were performed at BL8.0.1 of the Advanced Light Source (ALS), a DOE Office of Science User Facility, under contract no. DE-AC02-05CH11231. G.-H.L. acknowledges financial support from the ALS fellowship program.

Conflict of Interest

The authors declare no conflict of interest.

Author Contributions

B.X., Y.Z., M.S., and X.L. authors contributed equally to this work. X.L. from Pacific Northwest National Laboratory (PNNL) proposed the research. B.X. prepared the cathode material and carried out the electrochemical testing and data analysis. Y.Z. did the theoretical simulation with supervision of P.B.B. M.S. did the HAADF-STEM and 3D electron tomography characterization. X.L from Argonne National Laboratory (ANL) performed the mass spectrometry coupled with in situ-heated high-energy XRD under supervision of G.X. and K.A. G.-H.L. and W.Y. performed ex situ XAS and RIXS study. F.O., X.Y., and M.H.E. helped with material characterizations. D.R. oversaw the program activities. B.X., Y.Z., M.S., and X.L. from ANL contributed equally to this work. B.X., Y.Z., P.B.B., and X.L. wrote the manuscript with input from all other coauthors.

Data Availability Statement

The data that support the findings of this study are available from the corresponding author upon reasonable request.

Keywords

layered cathode materials, protonation, rock-salt phase, sodium-ion batteries

Received: August 17, 2023
Revised: November 21, 2023
Published online: December 22, 2023

[1] B. Xiao, X. Sun, *Adv. Energy Mater.* **2018**, *8*, 1802057.
[2] J.-M. Kim, X. Zhang, J.-G. Zhang, A. Manthiram, Y. S. Meng, W. Xu, *Mater. Today* **2021**, *46*, 155.
[3] H. Y. Asl, A. Manthiram, *Science* **2020**, *369*, 140.
[4] X. Qin, P. B. Balbuena, M. Shao, *J. Phys. Chem. C* **2019**, *123*, 14449.
[5] R. Benedek, M. M. Thackeray, A. Van De Walle, *Chem. Mater.* **2008**, *20*, 5485.
[6] J. Choi, E. Alvarez, T. A. Arunkumar, A. Manthiram, *Electrochem. Solid-State Lett.* **2006**, *9*, A241.
[7] X. Gu, J.-L. Liu, J.-H. Yang, H.-J. Xiang, X.-G. Gong, Y.-Y. Xia, *J. Phys. Chem. C* **2011**, *115*, 12672.
[8] K. Xu, *Chem. Rev.* **2014**, *114*, 11503.
[9] J. Song, B. Xiao, Y. Lin, K. Xu, X. Li, *Adv. Energy Mater.* **2018**, *8*, 1703082.
[10] L. Wang, A. Dai, W. Xu, S. Lee, W. Cha, R. Harder, T. Liu, Y. Ren, G. Yin, P. Zuo, J. Wang, J. Lu, J. Wang, *J. Am. Chem. Soc.* **2020**, *142*, 14966.
[11] F. Zhang, S. Lou, S. Li, Z. Yu, Q. Liu, A. Dai, C. Cao, M. F. Toney, M. Ge, X. Xiao, W.-K. Lee, Y. Yao, J. Deng, T. Liu, Y. Tang, G. Yin, J. Lu, D. Su, J. Wang, *Nat. Commun.* **2020**, *11*, 3050.
[12] T. Li, X.-Z. Yuan, L. Zhang, D. Song, K. Shi, C. Bock, *Electrochem. Energy Rev.* **2019**, *3*, 43.
[13] P. Yan, J. Zheng, J. Liu, B. Wang, X. Cheng, Y. Zhang, X. Sun, C. Wang, J.-G. Zhang, *Nat. Energy* **2018**, *3*, 600.
[14] J. Song, K. Wang, J. Zheng, M. H. Engelhard, B. Xiao, E. Hu, Z. Zhu, C. Wang, M. Sui, Y. Lin, D. Reed, V. L. Sprenkle, P. Yan, X. Li, *ACS Energy Lett.* **2020**, *5*, 1718.
[15] X. Ren, S. Chen, H. Lee, D. Mei, M. H. Engelhard, S. D. Burton, W. Zhao, J. Zheng, Q. Li, M. S. Ding, M. Schroeder, J. Alvarado, K. Xu, Y. S. Meng, J. Liu, J.-G. Zhang, W. Xu, *Chem* **2018**, *4*, 1877.
[16] X. Ren, X. Zhang, Z. Shadike, L. Zou, H. Jia, X. Cao, M. H. Engelhard, B. E. Matthews, C. Wang, B. W. Arey, X.-Q. Yang, J. Liu, J.-G. Zhang, W. Xu, *Adv. Mater.* **2020**, *32*, 2004898.
[17] P. Vassilaras, X. Ma, X. Li, G. Ceder, *J. Electrochem. Soc.* **2012**, *160*, A207.
[18] L. Wang, J. Wang, X. Zhang, Y. Ren, P. Zuo, G. Yin, J. Wang, *Nano Energy* **2017**, *34*, 215.
[19] M. H. Han, E. Gonzalo, M. Casas-Cabanas, T. Rojo, *J. Power Sources* **2014**, *258*, 266.
[20] L. E. Camacho-Forero, P. B. Balbuena, *Phys. Chem. Chem. Phys.* **2017**, *19*, 30861.
[21] T. M. Østergaard, L. Giordano, I. E. Castelli, F. Maglia, B. K. Antonopoulos, Y. Shao-Horn, J. Rossmeisl, *J. Phys. Chem. C* **2018**, *122*, 10442.
[22] Y. Zhang, Y. Katayama, R. Tatara, L. Giordano, Y. Yu, D. Fraggedakis, J. G. Sun, F. Maglia, R. Jung, M. Z. Bazant, Y. Shao-Horn, *Energy Environ. Sci.* **2020**, *13*, 183.
[23] M. Bianchini, M. Roca-Ayats, P. Hartmann, T. Brezesinski, J. Janek, *Angew. Chem. Int. Ed.* **2019**, *58*, 10434.
[24] W. Liu, P. Oh, X. Liu, M.-J. Lee, W. Cho, S. Chae, Y. Kim, J. Cho, *Angew. Chem. Int. Ed.* **2015**, *54*, 4440.
[25] D. H. Kim, J.-Y. Kim, J.-H. Park, S.-O. Kim, H.-S. Kim, K.-B. Kim, K. Y. Chung, *Ceramics International* **2022**, *48*, 19675.
[26] J. Kang, B. Han, *ACS Appl. Mater. Interfaces* **2015**, *7*, 11599.
[27] I. Aleksandrova, E. A. Medina, M. Karppinen, *J. Solid State Chem.* **2020**, *289*, 121478.
[28] T. Toma, R. Maezono, K. Hongo, *ACS Appl. Energy Mater.* **2020**, *3*, 4078.
[29] A. D. Robertson, P. G. Bruce, *Electrochem. Solid-State Lett.* **2004**, *7*, A294.
[30] X. Liu, G.-L. Xu, L. Yin, I. Hwang, Y. Li, L. Lu, W. Xu, X. Zhang, Y. Chen, Y. Ren, C.-J. Sun, Z. Chen, M. Ouyang, K. Amine, *J. Am. Chem. Soc.* **2020**, *142*, 19745.
[31] Y. Bi, J. Tao, Y. Wu, L. Li, Y. Xu, E. Hu, B. Wu, J. Hu, C. Wang, J.-G. Zhang, Y. Qi, J. Xiao, *Science* **2020**, *370*, 1313.
[32] P.-F. Wang, Y. You, Y.-X. Yin, Y.-G. Guo, *Adv. Energy Mater.* **2018**, *8*, 1701912.
[33] P. Yan, J. Zheng, M. Gu, J. Xiao, J.-G. Zhang, C.-M. Wang, *Nat. Commun.* **2017**, *8*, 14101.
[34] S. Sharifi-Asl, J. Lu, K. Amine, R. Shahbazian-Yassar, *Adv. Energy Mater.* **2019**, *9*, 1900551.
[35] B. Xiao, B. Wang, J. Liu, K. Kaliyappan, Q. Sun, Y. Liu, G. Dadheech, M. P. Balogh, L. Yang, T.-K. Sham, R. Li, M. Cai, X. Sun, *Nano Energy* **2017**, *34*, 120.
[36] Y. Wu, C. Ma, J. Yang, Z. Li, L. F. Allard, C. Liang, M. Chi, *J. Mater. Chem. A* **2015**, *3*, 5385.
[37] K. Dai, J. Wu, Z. Zhuo, Q. Li, S. Sallis, J. Mao, G. Ai, C. Sun, Z. Li, W. E. Gent, W. C. Chueh, Y.-D. Chuang, R. Zeng, Z.-X. Shen, F. Pan, S. Yan, L. F. J. Piper, Z. Hussain, G. Liu, W. Yang, *Joule* **2019**, *3*, 518.
[38] E. Hu, Q. Li, X. Wang, F. Meng, J. Liu, J.-N. Zhang, K. Page, W. Xu, L. Gu, R. Xiao, H. Li, X. Huang, L. Chen, W. Yang, X. Yu, X.-Q. Yang, *Joule* **2021**, *5*, 720.
[39] B. Xiao, X. Liu, X. Chen, G.-H. Lee, M. Song, X. Yang, F. Omenya, D. M. Reed, V. Sprenkle, Y. Ren, C.-J. Sun, W. Yang, K. Amine, X. Li, G. Xu, X. Li, *Adv. Mater.* **2021**, *33*, 2107141.
[40] S. Francis Amalraj, B. Markovsky, D. Sharon, M. Talianker, E. Zinigrad, R. Persky, O. Haik, J. Grinblat, J. Lampert, M. Schulz-Dobrick, A. Garsch, L. Burlaka, D. Aurbach, *Electrochim. Acta* **2012**, *78*, 32.
[41] A. D. Robertson, P. G. Bruce, *Chem. Commun.* **2002**, 2790.
[42] A. D. Robertson, P. G. Bruce, *Chem. Mater.* **2003**, *15*, 1984.
[43] Z. Chen, Y. Ren, E. Lee, C. Johnson, Y. Qin, K. Amine, *Adv. Energy Mater.* **2013**, *3*, 729.
[44] K. Zhang, B. Li, Y. Zuo, J. Song, H. Shang, F. Ning, D. Xia, *Electrochem. Energy Rev.* **2019**, *2*, 606.